Research
Textile Engineering—Article

A General Strategy to Electrospin Nanofibers with Ultrahigh Molecular Chain Orientation

Xian Wen [a], Jian Xiong [a], Zhaoyang Sun [a], Liming Wang [a,b,*], Jianyong Yu [c], Xiaohong Qin [a,b,*]

[a] Key Laboratory of Textile Science and Technology, Ministry of Education, College of Textiles, Donghua University, Shanghai 201620, China
[b] State Key Laboratory for Modification of Chemical Fibers and Polymer Materials, Donghua University, Shanghai 201620, China
[c] Innovation Center for Textile Science and Technology, Donghua University, Shanghai 201620, China

ARTICLE INFO

ABSTRACT

The degree of polymer chain orientation is a key structural parameter that determines the mechanical and physical properties of fibers. However, understanding and significantly tuning the orientation of fiber macromolecular chains remain elusive. Herein, we propose a novel electrospinning technique that can efficiently modulate molecular chain orientation by controlling the electric field. In contrast to the typical electrospinning method, this technique can piecewise control the electric field by applying high voltage to the metal ring instead of the needle. Benefiting from this change, a new electric field distribution can be realized, leading to a non-monotonic change in the drafting force. As a result, the macromolecular chain orientation of polyethylene oxide (PEO) nanofibers was significantly improved with a record-high infrared dichroic ratio. This was further confirmed by the sharp decrease in the PEO jet fineness of approximately 80% and the nanofiber diameter from 298 nm to 114 nm. Interestingly, the crystallinity can also be adjusted, with an obvious drop from 74.9% to 31.7%, which is different from the high crystallinity caused by oriented chains in common materials. This work guides a new perspective for the preparation of advanced electrospun nanofibers with optimal orientation–crystallinity properties, a merited feature for various applications.

© 2022 THE AUTHORS. Published by Elsevier LTD on behalf of Chinese Academy of Engineering and Higher Education Press Limited Company. This is an open access article under the CC BY-NC-ND license (http://creativecommons.org/licenses/by-nc-nd/4.0/).

1. Introduction

Molecular chain orientation is of considerable interest for explaining fiber properties, as it is related to the mechanical, thermal, electrical, and optical properties of materials [1–7]. Electrospinning has been accepted as a versatile and feasible technology to prepare ultrafine nanofibers. Underling electric filed force, the draw ratio of polymer solutions can reach five orders of magnitude, making it promising for material microstructure regulation [8–12]. To date, many approaches have been proposed to achieve the microscopic arrangement of electrospun nanofibers, such as incorporating additives [13], changing the collector [5,14] (e.g., drums, air gap electrodes, and discs), or stretching [15–17]. For example, Yano et al. [15] proposed that the orientation of molecular chains and crystallites can be improved by uniaxially stretching nanofibers. Kongkhlang et al. [5] proved that the chain orientation

characteristics could be affected by adjusting the rotating speed of the disk collector. Unfortunately, it is still extremely challenging to significantly regulate the orientation of nanofibers at the molecular level.

The electric field force is the main driving force for preparing electrospun nanofibers, which can affect jet formation, flow path, and stretching [18–20]. Recently, there has been growing interest in controlling the molecular orientation by regulating the electric field [21,22]. At the very beginning, the electric field induced device was designed by changing the collector to counter-electrode plates. As a result, the polymer chains were orientated along the fiber axis and the macroscopic arrangement of polymer nanofibers was realized [23]. Li et al. [24] designed different types of nozzles to control the electric field, thereby exploring the effect of electric field on the stretching of molecular chains. They found that a higher velocity at the initial jet could form fibers with higher degree of orientation. However, due to the inherent gradual attenuation trend of conventional electrospinning electric field from the spinneret outlet to collector, these methods are still had limited effect on regulation of molecular chain orientation.

* Corresponding authors.
  E-mail addresses: wangliming@dhu.edu.cn (L. Wang), xhqin@dhu.edu.cn (X. Qin).

Here, we designed a novel electrospinning technique by applying an electric field to the metal ring instead of the needle, which achieved separate control of the electric field. The separate-controlled electric field can tune the molecular chain orientation and crystallization of nanofibers. This change can be attribute to the special axial electric field distribution on the metal ring system (rising initially and then falling) which is different from the typical electrospinning technique. This phenomenon was verified by theoretical analysis and electric field simulations. Also, the scanning electron microscope (SEM) results showed that this technique can significantly stretch the straight segment jet. Benefits from the jet stretching, the nanofiber diameter, which was twice as fine as ordinary nanofibers, was also greatly reduced. In addition, we used polarized Fourier transform infrared spectroscopy (FTIR) and differential scanning calorimetry (DSC) to demonstrate that our technique alters fiber orientation and crystallization better than currently reported methods. These new understandings expand the ways to enhance the regulation of the macroscopic morphology and microstructure of electrospun nanofibers, and have guiding significance for the preparation of advanced fiber materials.

2. Materials and methods

2.1. Materials

Polyethylene oxide (PEO; average molecular weight (Mw) of 700 000 g·mol^{-1}) was purchased from Aladdin Reagent Co., Ltd. (China). Deionized water was prepared using laboratory water purification system (SMART-N; Canrex Analytic Instrument Co., Ltd., China). The vacuum-dried PEO powder was dissolved in deionized water under magnetic stirring for 12 h to obtain 5 wt% PEO spinning solution. The PEO cast film was obtained by spreading 5 wt% PEO spinning solution and dehydration under normal pressure.

2.2. Experimental methods

Schematic illustration of the novel electrospinning system and the typical electrospinning is displayed in Fig. 1(a). A new electric field control element (metal ring) was introduced to the novel electrospinning device and the positive electrode of the high-voltage generator (RR120-2P/DDPM/220; Gamma High Voltage Research, USA) was only connected to the metal ring. The syringe pump (LSP01-1A; LongerPump, China) was applied to inject the polymer solution into a 10 mL plastic syringe. In order to reduce the influence of gravity on Taylor cone, the spinning needles were arranged vertically to avoid asymmetric deformation of the spinning solution. The single needle is arranged on the axis of the metal ring. Compared with the typical electrospinning, the new electrospinning technology adds two adjustable parameters: ① radius R of the metal ring and ② relative position x of the needle (distance from the top of the needle to the plane of the ring). The novel electrospinning experiments were conducted with an applied voltage of 8 kV and the distance between the ring plane and the collector was set to 21 cm. The electric field can be controlled by adjusting the relative position x, specific details can find from Table S1 in Appendix A. For comparison, a typical electrospinning experiment was conducted with the same applied voltage and the working distance was varied according to the novel electrospinning working distance (Table S2 in Appendix A). The radius of the metal ring was fixed at 2 cm in this study, and the size of the single needle
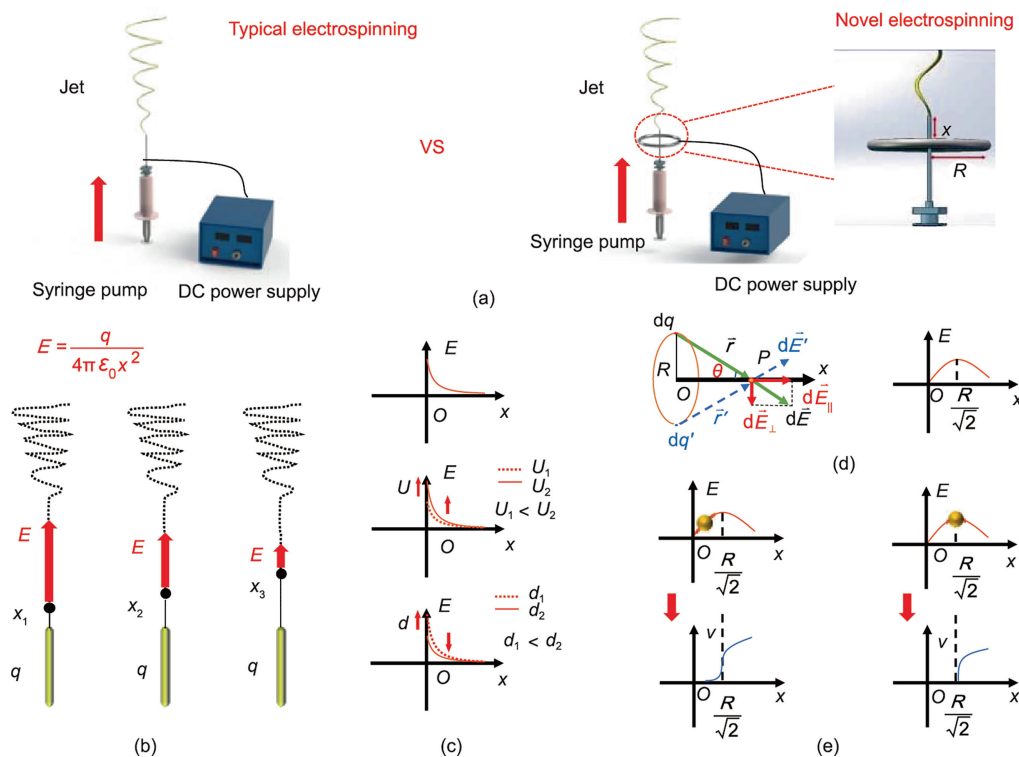
Fig. 1. (a) Schematic of typical electrospinning device (left) and novel electrospinning device (right). DC: direct current. (b) The state of electric field strength during typical electrospinning q: the total charge of the nozzle; $\varepsilon 0$: dielectric constant. (c) Electric field strength distribution along the direction of straight jet (top), and variation of electric field intensity by tuning applied voltage (middle) and working distance (bottom) U: applied voltage; d: spinning distance. (d) Analysis of electric field strength of novel electrospinning. q': the charge at the point on the ring; r': the distance from the point on the ring to a point on the straight segment; E': the electric field strength on the central axis generated by the point on the ring. (e) Electric field strength (up) and jet velocity (v) trend (bottom) of spinnerets equipped in different relative positions along the direction of jet motion; the relative distance between spinneret and metal ring meeting $x < \frac{R}{\sqrt{2}}$ (left) and $x \geq \frac{R}{\sqrt{2}}$ (right).

was 18G (inner diameter = 0.86 mm). All the experiments were fully supplied with liquid, and the flow rate of spinning solution was 2 mL·h^{-1}. The spinning environment was as follows: humidity of 50% ± 5% and temperature of (25 ± 2) °C.

2.3. Scanning electron microscopy of nanofibers

The morphology of the nanofibers was observed after spraying with platinum for 40 s at a current of 10 mA using SU8010 field emission scanning electron microscope (FE-SEM) from Hitachi, Japan. Subsequently, 100 fibers obtained from FE-SEM images were used to calculate the average fiber diameter by Image J software (National Institute of Health, USA). The average diameter ($\bar{d}$) and diameter coefficient of variation (CV) were calculated based on the above data.

2.4. Jet diameter measurement

To measure the jet diameter, a piece of slide glass was used to cut the jet at the same position as the straight segment, the detailed procedure can be found in Ref. [25] which shows this procedure with movie. Jet images were obtained by SEM after air drying. The average diameter of jets was determined based on directly measuring 30 jets by Image J software.

2.5. Molecular orientation characterization

Polarized FTIR was used to investigate molecular orientation in the nanofibers. The aligned nanofiber samples were collected using a hollow double-electrode plate, as shown in Fig. S1(a) in Appendix A. The parameters of the hollow double electrode plate are shown in Fig. S1(b) in Appendix A, and the material used was aluminum. For comparison, randomly arranged nanofiber samples were collected using a conventional flat plate device. Polarized infrared spectra of the samples were obtained using Fourier infrared spectrometer NEXUS-670 (Nicolet, USA). The samples were tested at 0° (parallel direction) and 90° (perpendicular direction), and the spectral collection range was 1500–800 cm^{-1}.

2.6. Differential scanning calorimetry

Thermal analysis was performed using a PerkinElmer DSC-4000 (USA) differential scanning calorimeter. Approximately 3 mg of the sample was added to an aluminum pan, and the heating and cooling procedures were performed under a nitrogen flow of 20 mL·min^{-1}. The specific procedure was to hold at 0 °C for 1 min, then to heat to 85 °C at a rate of 10 °C·min^{-1} and hold for 1 min, and finally to cool down to 0 °C at a rate of 10 °C·min^{-1}.

2.7. Electric field simulation

The three-dimensional (3D) electric fields generated by two the types of electrospinning were simulated using the electrostatics module of COMSOL Multiphysics Version 5.6 (Sweden). The electrostatic model is based on Laplace equations with proper boundary conditions [26]:

$$E = -\nabla V \tag{1}$$

where E is the electric field intensity and V is the electric potential. The physical geometries and properties of the electrospinning devices (needle, auxiliary ring, and collector) were established according to their practical dimensions and relative permittivity. In typical electrospinning, the high voltage of 8 kV was applied to the needle, whereas in novel electrospinning, it was applied to the ring. The receiving distance of both was set to 21 cm.

3. Results and discussion

3.1. Distribution of electric field strength

To clarify the electric field distribution via different electrospinning techniques (Fig. 1(a)), the theoretical and simulation analyses were performed. Assuming that the total charge of the nozzle is q, the dielectric constant is ε_0, thus the electric field strength at distance x (from the top of the needle to the plane of the ring) can be expressed as

$$E = \frac{q}{4\pi\varepsilon_0 x^2} \tag{2}$$

The spatial electric field strength distribution of typical electrospinning at different stages is shown in Fig. 1(b). The electric field strength decreases monotonically along the direction of jet motion in the straight segment. During the typical electrospinning process, the electric field can be adjusted by simply changing the applied voltage U or the spinning distance d. The variation in the electric field strength with the voltage and working distance is shown in Fig. 1(c). As the applied voltage U increases or the spinning distance d decreases, the electric field strength increases, but the monotonically decreasing trend remains constant. This is why the typical electric field strength distribution along the direction of straight segment jet is difficult to adjust significantly.

Fig. 1(d) shows the analysis of electric field strength on the central axis of the novel electrospinning (the direction of the jet in the straight segment). Since the charge is uniformly distributed on the metal ring, the axial electric field generated by the metal ring is given by the following derivation.

$$dE = \frac{dq}{4\pi\varepsilon_0 r^2} \tag{3}$$

$$\vec{E}_\perp = 0 \tag{4}$$

where r is the distance from a point on the straight segment to the ring.

The integral of Eq. (3) is expressed as

$$E = E_\parallel = \int dE_\parallel = \int dE\cos\theta = \int \frac{x}{r}dE = \int \frac{x}{r} \cdot \frac{dq}{4\pi\varepsilon_0 r^2}$$
$$= \int \frac{xdq}{4\pi\varepsilon_0 r^3} = \frac{qx}{4\pi\varepsilon_0 \left(x^2 + R^2\right)^{\frac{3}{2}}} \tag{5}$$

where θ is the angle between the central axis of the point and the ring.

Therefore, the partial derivative can be obtained as

$$\frac{dE(x)}{dx} = \frac{q\left[\left(x^2 + R^2\right)^{\frac{3}{2}} - 3x^2\left(x^2 + R^2\right)^{\frac{1}{2}}\right]}{4\pi\varepsilon_0\left(x^2 + R^2\right)^3} \tag{6}$$

The extremum point of the electric field strength $E(x)$ function can be obtained by Eq. (6), and is derived as follows

$$\frac{dE(x)}{dx} = \frac{q\left(x^2 + R^2\right)^{\frac{1}{2}}\left(R^2 - 2x^2\right)}{4\pi\varepsilon_0\left(x^2 + R^2\right)^3} = 0, \, x \geq 0, \, R > 0 \tag{7}$$

Therefore, when $x < \frac{R}{\sqrt{2}}$, $\frac{dE(x)}{dx} > 0$, the electric field strength increases monotonically as x increases; and when $x > \frac{R}{\sqrt{2}}$, $\frac{dE(x)}{dx} < 0$, the electric field strength decreases monotonically with an increase in x. The novel electrospinning method can provide a differentially distributed axial electric field compared with traditional electrospinning. By adjusting the relative position x, the jet

experienced different spatial electric fields. Taking $x = \frac{R}{\sqrt{2}}$ as the dividing point, the jet can experience two typical space electric fields, and the electric field strength distribution is shown in Fig. 1(d). Assuming that the charge of the jet is constant Q and the mass is constant m, the electric field force (F) and acceleration (a) of the jet in different stages are as follows:

$$F = EQ \tag{8}$$

$$a = F/m \tag{9}$$

It can be further deduced that the electric field force along the direction of the straight segment jet no longer monotonically decreases and the velocity change of the jet is controlled by the differential electric field. The golden yellow ball in Fig. 1(e) represents the electric field strength at the different relative distance x. The different positions of the golden ball correspond to the different motion states of the jet. As shown in Fig. 1(e), when the relative position $x < \frac{R}{\sqrt{2}}$, the electric field strength increases first and then falls. Correspondingly, the jet in the initial stage will first experience a variable acceleration motion with increased acceleration, which changes the inherent characteristics of the typical electrospinning jet with reduced acceleration. When the relative position $x > \frac{R}{\sqrt{2}}$, the electric field strength decreases monotonically like that of typical electrospinning process, and the jet directly enters the stage of decreasing acceleration. In addition, the length of the variable acceleration motion process of the acceleration increase can also be adjusted by changing x.

To further identify above result, we simulate the electric field strength distribution of these two electrospinning systems (Fig. 2). The z-direction in the simulation part represents the direction from the needle to the collector and the simulations were performed according to the experimental conditions. The arrows in Figs. 2(c) and (d) indicate the direction of the electric field at that position, and their length is proportional to the electric field strength. Typical electrospinning only produces a high electric field at the outlet of the spinneret (Fig. 2(c)); while a stronger and more uniform electric field is generated by novel electrospinning at a distance of several millimeters from the outlet of the spinneret (Fig. 2(d)). The trend of electric field distribution could be revealed by quantitatively analyzing of the established model, as shown in Figs. 2(e) and (f). The centerline electric field strength along the z-axis of the typical electrospinning gradually attenuation from the outlet of spinneret. Nevertheless, the novel electrospinning changes the trend of monotonous decrease and creates a differentiated electric field distribution, which is consistent with our previous theoretical analysis shown in Fig. 1.

### 3.2. Characteristics of jet diameter and nanofibers diameter

To demonstrate the influence of the new electric field distribution on the jet, a series of experiments were performed under different separation control parameters, where the relative position of the nozzle x was controlled below $\frac{R}{\sqrt{2}}$. PEO, which is biofriendly, low-cost, and widely used in many fields was chosen to investigate its actual effect on jet distribution [13]. The samples were obtained by cutting jet at the same position of straight segment, as shown in Fig. 3. According to the different relative positions x of the rings, the samples of novel electrospinning and typical electrospinning are named 1#–5# and 6#–10#, respectively (Tables S1 and S2). The samples 1#–5# indicate different relative distance x: $\frac{\sqrt{2}}{16}R$, $\frac{\sqrt{2}}{8}R$, $\frac{\sqrt{2}}{4}R$, $\frac{3\sqrt{2}}{8}R$, and $\frac{\sqrt{2}}{2}R$. The corresponding working distance also varies with the relative distance x. As control, typical electrospinning samples 6#–10# were prepared at the same collection distances corresponding to 1#–5#. It is evident that the new electric field distribution can prominently reduce the jet fineness by approximately 80% compared with the SEM image of 1#
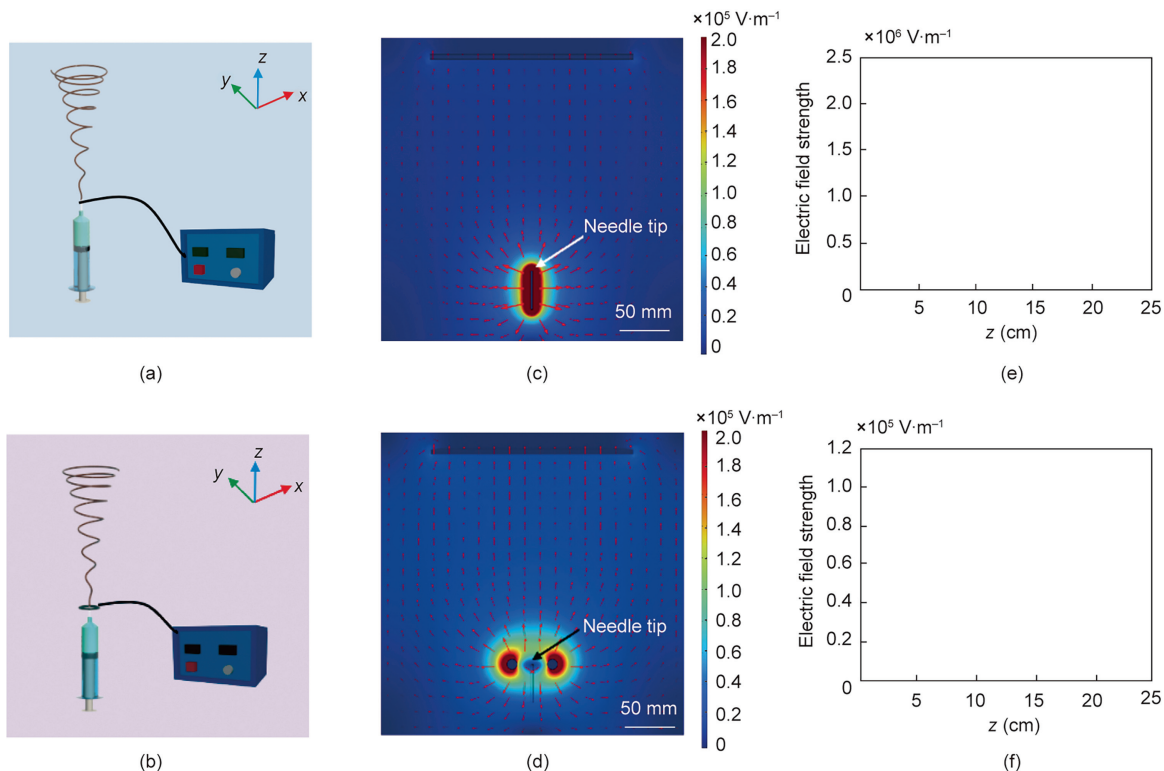
Fig. 2. Schematic of 3D model of (a) typical electrospinning setup and (b) novel electrospinning. Electric field distributions of (c) typical electrospinning and (d) novel electrospinning. Centerline electric field strength for (e) typical electrospinning and (f) novel electrospinning with an applied voltage of 8 kV and a working distance of 21 cm.
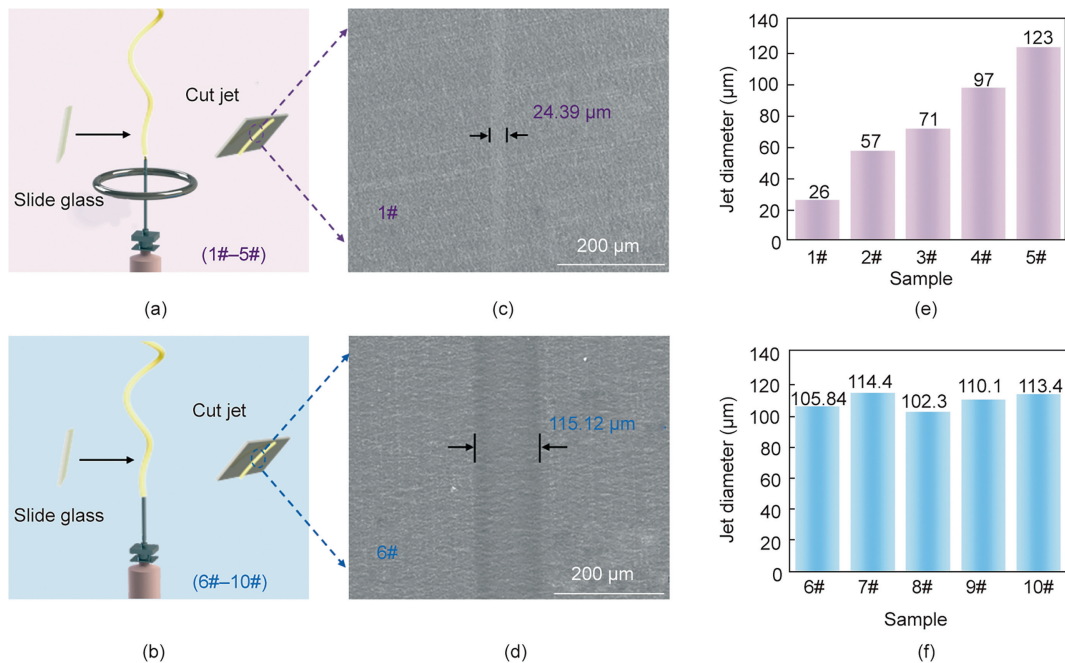
Fig. 3. Schematic diagram of cut jet by (a) novel electrospinning and (b) typical electrospinning. SEM images of jets in straight section at same position via (c) novel electrospinning and (d) typical electrospinning. (e) The jet diameter of novel electrospun nanofibers with different control parameters. (f) Jet diameter of typical electrospun nanofibers with different control parameters. The real values of the working distance of 1#–5# and 6#–10# are 20.823, 20.646, 20.293, 19.939, and 19.586 cm, respectively.
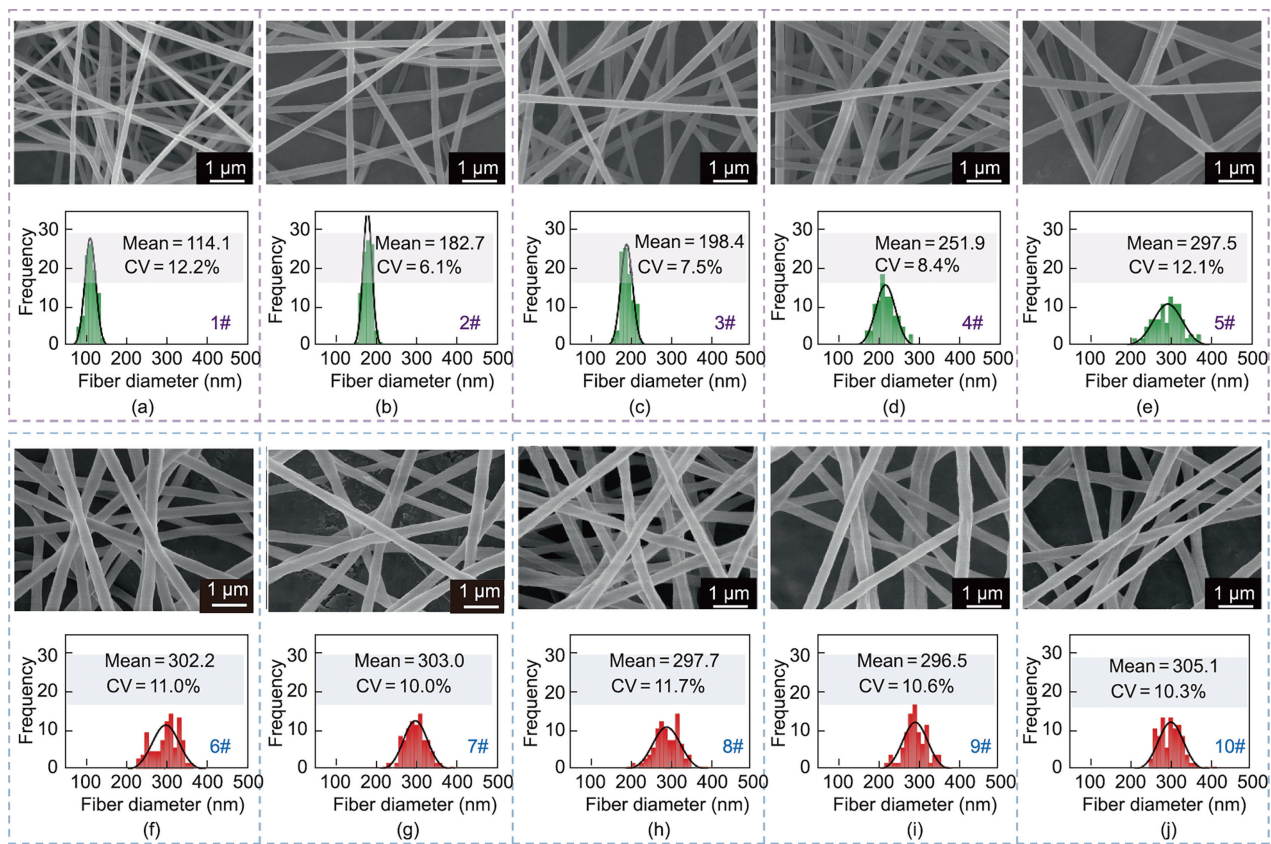

Fig. 4. (a–e) SEM images and diameter distributions of nanofibers via novel electrospinning with different control parameters: (a) 1#, (b) 2#, (c) 3#, (d) 4#, and (e) 5#. (f–j) SEM images and diameter distributions of nanofibers via typical electrospinning with different working distances: (f) 6#, (g) 7#, (h) 8#, (i) 9#, and (j) 10#.

(Fig. 3(c)) and 6# (Fig. 3(d)) cutting the jets under same applied voltage and working distance. And Fig. 3(e) manifested that the jet diameter reduces significantly with the decrease of relative position x. In addition, as shown in Fig. 3(f), the control experiments of typical electrospinning show that increasing the overall electric field strength by adjusting the working distance cannot effectively refine the jet. Sample 5# exhibited jet fineness similar to that of the typical electrospinning. This might be because when $x \geq \frac{R}{\sqrt{2}}$, the jet directly enters the variable acceleration motion stage with reduced acceleration from the outlet of the spinneret, which is as same as that of the typical electrospinning. Above results reveal that the effective refinement of the jet could be

mainly attributed to two aspects: On the one hand, as the relative position x decreases, the initial force of the ejected jet reduces, making the volume of the drawn jet reduction, and the jet becomes thinner; on the other hand, with the decreased relative position x, the variable-acceleration motion process experienced by the jet increases, resulting in a rapid increase in the jet velocity, and the jet with lower initial viscosity obtains sufficient stretch refinement.

The morphologies and diameter distributions of PEO nanofibers under different control parameters of two electrospinning techniques are exhibited in Fig. 4. As the jet can be adjusted by varying the electric field, thus changing the relative position x can also
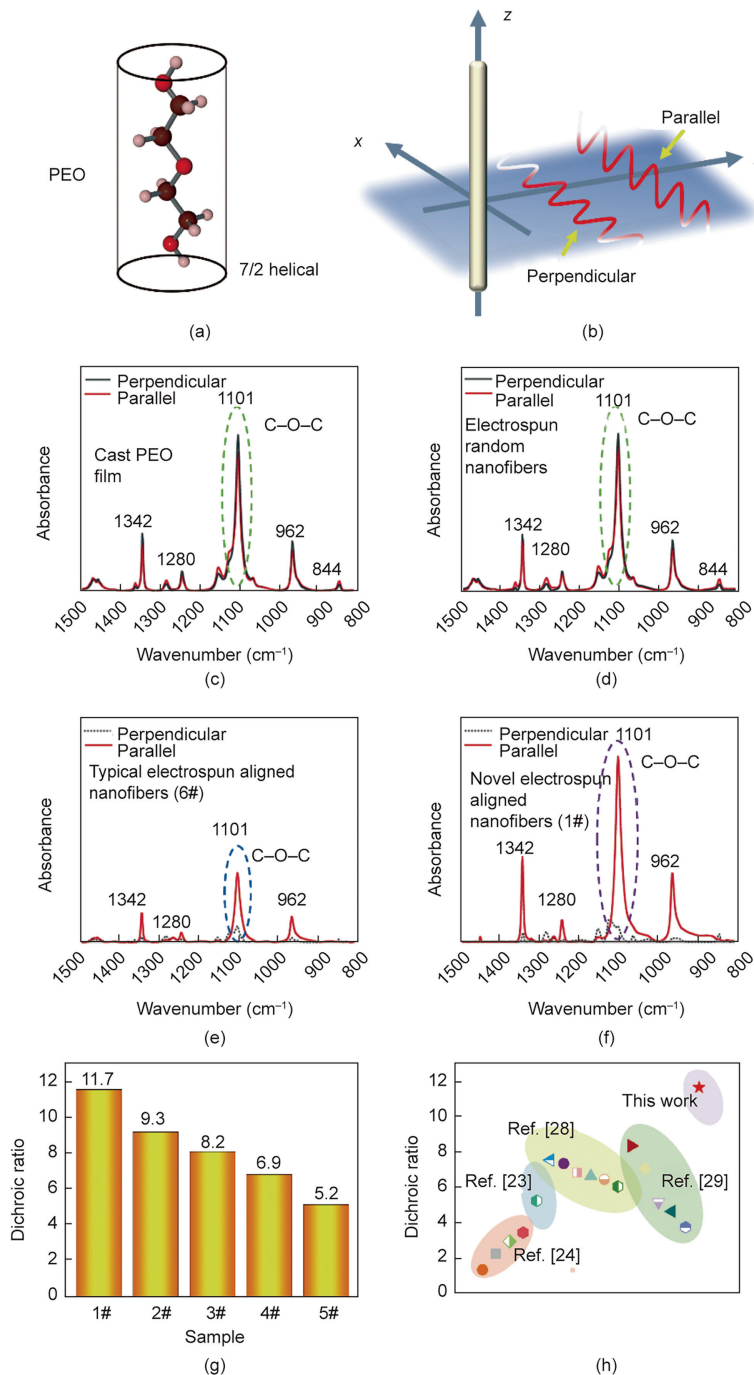
Fig. 5. (a) Macromolecular conformation of PEO. (b) Schematic diagram of polarization spectra parallel and perpendicular to fiber axis. Polarization infrared absorption of (c) cast PEO film, (d) electrospun random nanofibers, (e) typical electrospun aligned nanofibers (6#), and (f) novel electrospun aligned nanofibers (1#). (g) The infrared dichroic ratios of novel electrospun nanofibers with different control parameters. (h) The infrared dichroic ratios of PEO electrospun nanofibers reported in the existing literature.

effectively control the diameter of the nanofibers. With the relative position x decreasing, the fibers diameter decreased significantly from 298 nm to 114 nm. Besides, the CV values of novel electrospun nanofiber diameters reduced from 12.2% to 6.1%; however, when x is $\frac{\sqrt{2}}{16}R$, the CV value explodes to 12.2%. This could be attributed to the excitation force of jet being too small at this position, resulting in the reduction of jet excitation stability. As illustrated in Figs. 4(f)–(j), the overall electric field strength increase has little effect on nanofiber diameter. In conclusion, compared with typical electrospinning, the novel electrospinning performed better in controlling the stretching of the jet and refining of nanofibers. And the smaller the x, the better the effect. In addition, we also studied the thermal stability of the prepared PEO nanofibers. The results turned that the PEO nanofibers did not have much change when treated it with a temperature of approximately 55 °C for 3 h (Fig. S2 in Appendix A). While, further increase the temperature (above 60 °C for 3 h) will make the membrane melt, as the temperature is close to the melting temperature of PEO.

3.3. Orientation of nanofiber macromolecular chains

Having elucidated the effect of the electric field distribution on jet stretching, the molecular chain orientation of the nanofiber was further investigated. Polarized FTIR spectra mainly reflects the molecule functional groups through the absorption spectrum of materials, which are applied to study the characteristic of molecular orientation. The PEO molecular chain is composed of –CH_2–CH_2–O– repeating units and has a linear 7/2 helical structure (Fig. 5(a)). There are large number of C–O–C bonds and C–H bonds along the PEO linear macromolecular chain direction, causing absorbance intensities at specific wavelengths. When the macromolecular chain is oriented along the fiber axis, the absorption spectrum along the parallel direction and the perpendicular direction of the fiber axis will be significantly different (Fig. 5(b)). The characteristic infrared bands of the 1101 cm^{-1} peak are attributed to the C–O–C stretching vibration, which is along the backbone of the macromolecular chain and is relatively independent. Therefore, it can be used to analyze the degree of PEO macromolecular chain orientation.

As shown in Figs. 5(c) and (d), the polarized FTIR spectra of the cast PEO film and electrospun random nanofibers almost completely overlapped in two perpendicular directions, indicating that the material exhibits good isotropic characteristics. A significant absorbance differences of the typical electrospun and novel electrospun aligned nanofibers was observed from polarized FTIR spectra of two mutually perpendicular directions. According to the absorbance at 1101 cm^{-1} band (Figs. 5(e) and (f)), the novel electrospun nanofibers exhibit higher polarization absorbance differences, which indicates that nanofibers with higher macromolecular chain orientation were prepared. Moreover, to further clarify the molecular chain orientation characteristics and influence mechanism of novel electrospun nanofibers, polarization-infrared characterizations of novel electrospun nanofibers under different parameters were carried out (Fig. S3 in Appendix A). The absorbance height of the 1101 cm^{-1} band perpendicular to the fiber axis is unified in all polarization spectra. As shown in Fig. 5(g), the degree of macromolecular chain orientation of PEO fibers can be significantly regulated by changing the separate control parameters.

To quantify the degree of PEO macromolecular orientation, the infrared dichroic ratios (D) of the 1101 cm^{-1} band can be expressed by the following equation.

$$D = \frac{P_\parallel}{P_\perp} \tag{10}$$

where the $P_\parallel$ is the parallelly polarized infrared absorbance intensity at 1101 cm^{-1}, and $P_\perp$ represents the perpendicular polarized infrared absorbance intensity at 1101 cm^{-1}. Fig. 5(g) shows the infrared dichroic ratio of nanofibers with different novel electrospinning parameters. The higher the D value, the better alignment of the chains along the fiber axis [27]. When the relative position x decreases, the infrared dichroic ratios of the novel electrospinning nanofibers improved. Compared with previous studies, the PEO nanofibers with the highest infrared dichroic ratio (11.7) were prepared by novel electrospinning (Fig. 5(h)) [23,24,28,29]. The ultrahigh infrared dichroic ratios confirmed that the electric field strength distribution has an essential effect on the macromolecular chain orientation of the electrospun nanofibers. By controlling the electric field separately, the stretching and refining process of the jet can be regulated, and nanofibers with adjustable macromolecular chain orientation can be obtained [30]. The smaller the relative position x, the more vigorous stretching of the polymer jet in the straight segment, resulting in a higher degree of molecular chain orientation.

3.4. Crystallization properties of nanofibers

Controlling the crystallization behavior of polymers is of paramount importance since it largely determines their final properties. Fig. 6(a) shows the DSC curve for the prepared nanofibers. Thought the temperature point T_m of the PEO nanofibers is concentrated at around 70 °C, the T_m of 1# has a significant decrease compared with 6#, which may be attributed to the decrease in the average fiber diameter [31]. The crystallinity X_c of the PEO nanofiber film can be calculated by $X_c = \frac{\Delta H_m}{\Delta H_\infty}$, where
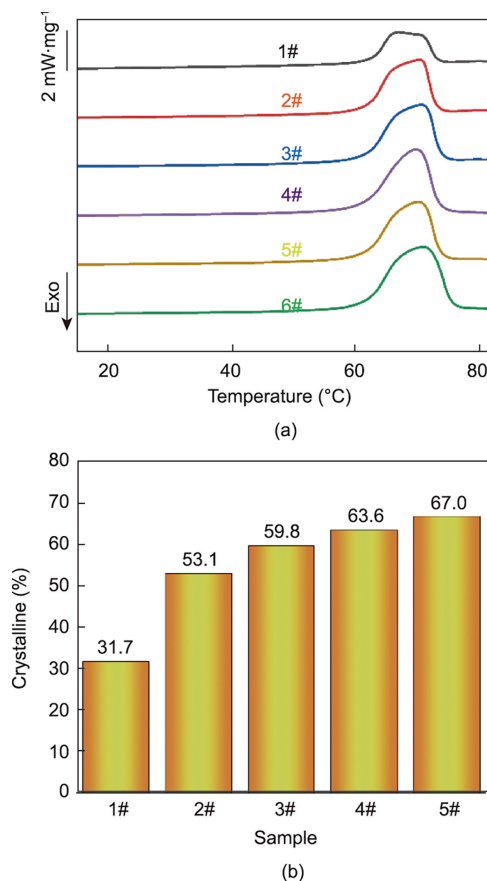

Fig. 6. (a) DSC thermograms and (b) crystalline of novel electrospun nanofibers with different control parameters. Exo: exotherm.

$\Delta H_{\rm m}$ is the melting enthalpy of PEO nanofibers and ΔH_{∞} is the melting enthalpy of PEO with 100% crystallization [32]. The melting enthalpy of each sample was determined by integrating the melting peak. When x is $\frac{\sqrt{2}}{16}R$, $\frac{\sqrt{2}}{8}R$, $\frac{\sqrt{2}}{4}R$, $\frac{3\sqrt{2}}{8}R$, and $\frac{\sqrt{2}}{2}R$, the melting enthalpy of nanofibers is 62.3, 104.5, 117.5, 125.0, and 131.7 $J\cdot g^{-1}$, respectively, and the corresponding crystallinity are shown in Fig. 6(b). It can be found that the melting enthalpy of the novel electrospinning nanofibers decreases significantly with the relative distance decrease, indicating that the corresponding samples have lower crystallinity. For comparison, the melting enthalpy of the typical electrospun nanofibers was 147.27 $J\cdot g^{-1}$ and the crystallinity was 74.9%, which is much higher than the 31.7% crystallinity in novel electrospun PEO nanofibers. This relationship shows that the crystallinity of nanofibers can also be effectively tuned. Low crystallinity of the novel electrospun nanofibers may be ascribed to the quicker solvent evaporation in smaller jets, leading to rapid jet solidification that precludes polymer crystallization, despite its beneficial to chain orientation in nanofibers [1,33].

4. Conclusions

In conclusion, a novel electrospinning technique is proposed to efficiently tune molecular chain orientation by controlling the electric field. Theoretical analysis and simulation results revealed that the novel electrospinning technique could provide a differential electric field distribution, thereby resulting in a non-monotonic variation of drafting force. The variable acceleration draft with increased acceleration in the initial stage is responsible for jet refinement. By adjusting the position of the separate-control ring, the jet fineness can be effectively reduced by about 80% and the nanofiber diameter can be significantly decreased by approximately half. Furthermore, by changing the control parameters of novel electrospinning, the macromolecular chain orientation of PEO nanofibers could be significantly improved, and PEO nanofibers with ultrahigh infrared dichroic ratio (11.7) were prepared. Besides, we also note that the crystallinity of the novel electrospun PEO nanofibers can be as low as 31.7% compared with the typical electrospun fibers. This feasible and facile technology offers new insight into understanding and regulating the distribution of electrospinning electric fields, and provides a powerful tool to control the molecular orientation in nanofibers, which is vital for comprehending the processing–structure–property relationship of electrospun nanofibers.

Compliance with ethics guidelines

Xian Wen, Jian Xiong, Zhaoyang Sun, Liming Wang, Jianyong Yu, and Xiaohong Qin declare that they have no conflict of interest or financial conflicts to disclose.

Appendix A. Supplementary data

Supplementary data to this article can be found online at https://doi.org/10.1016/j.eng.2022.09.008.

References

[1] Papkov D, Zou Y, Andalib MN, Goponenko A, Cheng SZD, Dzenis YA. Simultaneously strong and tough ultrafine continuous nanofibers. ACS Nano 2013;7(4):3324–31.
[2] Papkov D, Pellerin C, Dzenis YA. Polarized Raman analysis of polymer chain orientation in ultrafine individual nanofibers with variable low crystallinity. Macromolecules 2018;51(21):8746–51.
[3] Deng L, Chen G. Recent progress in tuning polymer oriented microstructures for enhanced thermoelectric performance. Nano Energy 2021;80:105448.
[4] Liu Y, Pellerin C. Highly oriented electrospun fibers of self-assembled inclusion complexes of poly(ethylene oxide) and urea. Macromolecules 2006;39 (26):8886–8.
[5] Kongkhlang T, Tashiro K, Kotaki M, Chirachanchai S. Electrospinning as a new technique to control the crystal morphology and molecular orientation of polyoxymethylene nanofibers. J Am Chem Soc 2008;130(46):15460–6.
[6] Laramée AW, Lanthier C, Pellerin C. Electrospinning of highly crystalline polymers for strongly oriented fibers. ACS Appl Polym Mater 2020;2 (11):5025–32.
[7] Yang Y, Li X, Mi J, Ramakrishna S, Ji D, Yu J, et al. Coordinating chain crystallinity and orientation by tailoring electrical stretching for fabrication of super-tough and strong organic fibers. Chem Eng J 2022;442:136203.
[8] Xue J, Wu T, Dai Y, Xia Y. Electrospinning and electrospun nanofibers: methods, materials, and applications. Chem Rev 2019;119(8):5298–415.
[9] Richard-Lacroix M, Pellerin C. Molecular orientation in electrospun fibers: from mats to single fibers. Macromolecules 2013;46(24):9473–93.
[10] Papkov D, Delpouve N, Delbreilh L, Araujo S, Stockdale T, Mamedov S, et al. Quantifying polymer chain orientation in strong and tough nanofibers with low crystallinity: toward next generation nanostructured superfibers. ACS Nano 2019;13(5):4893–927.
[11] Wen X, Xiong J, Lei SL, Wang LM, Qin XH. Diameter refinement of electrospun nanofibers: from mechanism, strategies to applications. Adv Fiber Mater 2022;4(2):145–61.
[12] Fang F, Wang H, Wang H, Huang WM, Chen Y, Cai N, et al. Stimulus-responsive shrinkage in electrospun membranes: fundamentals and control. Micromachines 2021;12(8):920.
[13] Wang Y, Li M, Rong J, Nie G, Qiao J, Wang H, et al. Enhanced orientation of PEO polymer chains induced by nanoclays in electrospun PEO/clay composite nanofibers. Colloid Polym Sci 2013;291(6):1541–6.
[14] Richard-Lacroix M, Pellerin C. Raman spectroscopy of individual poly(ethylene oxide) electrospun fibers: effect of the collector on molecular orientation. Vib Spectrosc 2017;91:92–8.
[15] Yano T, Higaki Y, Tao Di, Murakami D, Kobayashi M, Ohta N, et al. Orientation of poly(vinyl alcohol) nanofiber and crystallites in non-woven electrospun nanofiber mats under uniaxial stretching. Polymer 2012;53(21):4702–8.
[16] Tian D, He JH. Control of macromolecule chains structure in a nanofiber. Polymers 2020;12(10):2305.
[17] Song Z, Hou X, Zhang L, Wu S. Enhancing crystallinity and orientation by hot-stretching to improve the mechanical properties of electrospun partially aligned polyacrylonitrile (PAN) nanocomposites. Materials 2011; 4(4):621–32.
[18] Hao S, Pingjuan N, Pingfan N. The auxiliary electrode can improve the electric field distribution of the roller electrostatic spinning. IOP Conf Ser Earth Environ Sci 2019;358(5):052077.
[19] Li X, Bian FG, Lin JY, Zeng YC. Effect of electric field on the morphology and mechanical properties of electrospun fibers. RSC Adv 2016; 6(56):50666–72.
[20] Niu HT, Lin T, Wang XG. Needleless electrospinning. I. A comparison of cylinder and disk nozzles. J Appl Polym Sci 2009;114(6):3524–30.
[21] Lin DY, Martin DC. Orientation development in electrospun liquid–crystalline polymer nanofibers. Polymeric Nanofibers 2006;918:330–42.
[22] Richard-Lacroix M, Pellerin C. Orientation and partial disentanglement in individual electrospun fibers: diameter dependence and correlation with mechanical properties. Macromolecules 2015;48(13):4511–9.
[23] Kakade MV, Givens S, Gardner K, Lee KH, Chase DB, Rabolt JF. Electric field induced orientation of polymer chains in macroscopically aligned electrospun polymer nanofibers. J Am Chem Soc 2007;129(10):2777–82.
[24] Li X, Lin J, Zeng YC. Electric field distribution and initial jet motion induced by spinneret configuration for molecular orientation in electrospun fibers. Eur Polym J 2018;98:330–6.

[25] Lei S, Xiong C, Quan Z, Qin X, Yu J. Controlled stretching of the first spiral in electrospinning whipping jet via surface charge. Polymer 2021;217: 123443.

[26] Gupta A, Ayithapu P, Singhal R. Study of the electric field distribution of various electrospinning geometries and its effect on the resultant nanofibers using finite element simulation. Chem Eng Sci 2021;235:116463.

[27] Pai CL, Boyce MC, Rutledge GC. Mechanical properties of individual electrospun PA 6(3)T fibers and their variation with fiber diameter. Polymer 2011;52(10):2295–301.

[28] Song Z, Chiang SW, Chu X, Du H, Li J, Gan L, et al. Effects of solvent on structures and properties of electrospun poly(ethylene oxide) nanofibers. J Appl Polym Sci 2018;135(5):45787.

[29] Lu C, Chiang SW, Du H, Li J, Gan L, Zhang X, et al. Thermal conductivity of electrospinning chain-aligned polyethylene oxide (PEO). Polymer 2017;115:52–9.

[30] Greenfeld I, Fezzaa K, Rafailovich MH, Zussman E. Fast X-ray phase-contrast imaging of electrospinning polymer jets: measurements of radius, velocity, and concentration. Macromolecules 2012;45(8):3616–26.

[31] Wang W, Barber AH. Diameter-dependent melting behaviour in electrospun polymer fibres. Nanotechnology 2010;21(22):225701.

[32] Pielichowski K, Flejtuch K. Phase behavior of poly(ethylene oxide) studied by modulated-temperature DSC—influence of the molecular weight. J Macromol Sci B 2004;43(2):459–70.

[33] Wu X-F, Salkovskiy Y, Dzenis YA. Modeling of solvent evaporation from polymer jets in electrospinning. Appl Phys Lett 2011;98(22):223108.